Clathrin light chain diversity regulates membrane deformation in vitro and synaptic vesicle formation in vivo

Lisa Redlingshöfer[a,b], Faye McLeod[c,1], Yu Chen[a,b], Marine D. Camus[a,b], Jemima J. Burden[d], Ernest Palomer[c], Kit Briant[a,b], Philip N. Dannhauser[a,b,2], Patricia C. Salinas[c], and Frances M. Brodsky[a,b,3]

[a]Research Department of Structural and Molecular Biology, Division of Biosciences, University College London, London WC1E 6BT, United Kingdom; [b]Institute of Structural and Molecular Biology, Birkbeck and University College London, London WC1E 7HX, United Kingdom; [c]Research Department of Cell and Developmental Biology, Division of Biosciences, University College London, London WC1E 6BT, United Kingdom; and [d]Medical Research Council Laboratory for Molecular Cell Biology, University College London, London WC1E 6BT, United Kingdom

Clathrin light chain (CLC) subunits in vertebrates are encoded by paralogous genes *CLTA* and *CLTB*, and both gene products are alternatively spliced in neurons. To understand how this CLC diversity influences neuronal clathrin function, we characterized the biophysical properties of clathrin comprising individual CLC variants for correlation with neuronal phenotypes of mice lacking either CLC-encoding gene. CLC splice variants differentially influenced clathrin knee conformation within assemblies, and clathrin with neuronal CLC mixtures was more effective in membrane deformation than clathrin with single neuronal isoforms nCLCa or nCLCb. Correspondingly, electrophysiological recordings revealed that neurons from mice lacking nCLCa or nCLCb were both defective in synaptic vesicle replenishment. Mice with only nCLCb had a reduced synaptic vesicle pool and impaired neurotransmission compared to WT mice, while nCLCa-only mice had increased synaptic vesicle numbers, restoring normal neurotransmission. These findings highlight differences between the CLC isoforms and show that isoform mixing influences tissue-specific clathrin activity in neurons, which requires their functional balance.

clathrin | membrane traffic | coated vesicle formation | protein isoforms | neuronal synapse

Clathrin mediates vesicle formation from the plasma membrane and endosomal compartments (1). Recruited by cargo-recognizing adaptor proteins, triskelion-shaped clathrin proteins assemble into polyhedral lattices to capture membrane-associated cargo and promote membrane bending into clathrin-coated vesicles (CCVs). Through sequestration of a variety of cargo, CCVs play fundamental roles in general cellular physiology, including regulation of nutrient uptake and signaling, as well as in tissue-specific membrane traffic, such as synaptic vesicle (SV) generation (2). This range of clathrin functions has been attributed to adaptor and accessory protein variation (3). However, functional diversity is also generated by variability of clathrin subunits. Vertebrates have two types of clathrin heavy chains with distinct functions (4). The major vertebrate clathrin is formed from clathrin heavy chain CHC17 (herein referred to as CHC) associated with clathrin light chains (CLCs), which do not bind the minor CHC22 clathrin isoform. Vertebrate CLCs are encoded by two different genes, *CLTA* and *CLTB* (in humans), producing CLCa and CLCb isoforms of about 60% sequence identity (5, 6). Their sequence differences have been conserved during evolution, after the encoding genes arose through duplication, suggesting the two isoforms can mediate distinct functions (7, 8). Expression levels of the CLCa and CLCb isoforms are tissue-specific (9), and further variation is created by alternative gene splicing during development (10) and in the brain (5, 6). Here we address how CLC diversity affects the biophysical properties of clathrin and how the resulting variation affects the specialized function of clathrin in SV replenishment.

Limited functional differences between CLCa and CLCb have been observed in cell culture with respect to clathrin dynamics (11), during focal adhesion formation (12), cancer cell migration (13), and in epithelial polarity (14), with mechanisms attributed to isoform-specific differences in CLC binding proteins and posttranslational modification (15). Loss of CLCs in culture and in vivo affects CCV uptake of some, but not all cargo, possibly reflecting variability in mechanical demand for packaging different cargo into CCVs (9, 15, 16). The capacity for biophysical differences in clathrin comprising different CLC isoforms and their splicing variants to influence tissue-specific clathrin functions has not yet been considered. CLC variability has potential to affect clathrin function as CLCs interact with key domains of the clathrin triskelion that contribute to clathrin-mediated membrane bending. They bind the trimerization domain (TxD) at the triskelion vertex where the three component CHCs interact (17, 18), and extend along the triskelion leg to the bend at the knee where CLCs regulate conformation (19). Like various other endocytic proteins (3), CLCs undergo neuron-specific splicing (20), which introduces one exon in CLCb (encoding 18 residues) and two exons in CLCa (encoding 30 residues) at equivalent positions near the CLC C termini, resulting in higher molecular-weight forms nCLCb and nCLCa (5, 6), suggesting neuron-specific functions for these variants. In vitro, CLCs are required for efficient clathrin-mediated membrane vesiculation

Significance

This study reveals that diversity of clathrin light chain (CLC) subunits alters clathrin properties and demonstrates that the two neuronal CLC subunits work together for optimal clathrin function in synaptic vesicle formation. Our findings establish a role for CLC diversity in synaptic transmission and illustrate how CLC variability expands the complexity of clathrin to serve tissue-specific functions.

BIOCHEMISTRY

at low temperature (21). Thus, CLCs could affect clathrin-mediated membrane deformation directly through their influence on clathrin lattice properties (21, 22), as well as indirectly through cellular interaction with proteins that influence the actin cytoskeleton (14, 23–25).

SV replenishment by membrane traffic following neuronal degranulation is critical for sustained neurotransmission. Endocytosis is required to regulate synaptic plasma membrane surface area and to retrieve SV proteins (26), and SVs are generated from the plasma membrane and endosome-like compartments (27). The essential sites of clathrin function in these pathways are debated (2, 28), but dysfunction of clathrin-associated endocytic proteins is associated with neurological defects observed in Parkinson's disease (29), Alzheimer's disease (3), and in numerous animal models in which such proteins have been genetically deleted (30–35).

Here, we assess how clathrin lattices formed with neuronal and nonneuronal CLC variants could differentially affect function by correlating their in vitro biophysical properties with in vivo neuronal phenotypes of mice lacking CLC-encoding genes. We found that CLC composition significantly influenced clathrin lattice properties and the ability to form vesicles. CLC splice variation impacted assembly curvature by regulating CHC knee conformation, resulting in decreased ability of individual neuronal splice variants to deform liposome membrane in vitro. This effect was ameliorated for lattices formed from a mixture of neuronal CLC isoforms. Mice lacking either CLCa or CLCb isoforms showed corresponding differences in SV replenishment and synaptic neurotransmission compared to their WT littermates expressing both isoforms, and to each other. Collectively, these functional differences between CLC isoforms observed in vitro and in vivo establish a role for CLC diversity in regulating clathrin function in neurons and suggest a critical role for isoform balance.

Results

CLC Splice Variants Differentially Influence Lattice Curvature via the Triskelion Knee.
Within clathrin lattices, the knee bending angle determines whether a hexagon (noncurvature inducing) or pentagon (curvature-inducing) is formed (36, 37). In addition, the characteristic pucker at the triskelion vertex and the crossing angle of interacting CHC legs can further modulate lattice curvature (38, 39) (Fig. 1A). This versatility of clathrin assemblies allows clathrin to sequester cargo of various sizes, as well as to form stable, flat assemblies that serve as signaling hubs (3, 40). For each closed cage, there is a fixed number of 12 pentagons, but a varying number of hexagons (41) (Fig. 1A). Thus, larger cages (i.e., lattices of lower curvature) have a smaller pentagon-to-hexagon ratio. CLCs maintain the puckered conformation of triskelia in flat assemblies (21) and structural studies showed that nCLCb can influence conformation of the triskelion knee up to a degree that inhibits assembly (19). Considering these effects on CHCs, we hypothesized that sequence differences between the CLC isoforms and alterations due to splicing might modulate CLC influence on triskelion conformation and lattice curvature.

To address this, we produced clathrin triskelia of defined CLC composition by reconstituting tissue-derived CHC triskelia (42) with recombinantly expressed CLCa, CLCb, nCLCa, or nCLCb (*SI Appendix*, Fig. S1 *A–D*). We then induced assembly of these different clathrins into closed cages and analyzed cage diameter as a measure of lattice curvature by electron microscopy (EM). Previous studies showed that tissue-derived, CLC-bound clathrin (native) forms two major size classes, while CHC-only triskelia predominantly form small-sized cages (43–46). Our results confirmed that without CLCs, CHC formed predominantly cages of less than 90 nm in diameter, with an average size of around 70 nm, representing cages of up to 60 triskelia (45). Clathrin with

each of the CLC variants was further able to form larger cages with an average diameter of around 110 nm (140 triskelia) for those cages. The degree to which larger cages were formed varied significantly between splice variants (Fig. 1 *B* and *C*), indicating that the neuronal splice inserts regulate the influence of CLCs on lattice curvature.

To establish whether differences in larger cage formation resulted from CLC influence on the triskelion vertex or on the CHC knee conformation or both, we dissected the effect of CLCs separately for each domain. To test whether CLC diversity exerts influence through varying CHC knee conformation, we produced clathrin cages from two CHC fragments that together constitute a full-length clathrin triskelion "cut" at the knee (Fig. 1D) (47). The Hub fragment (residues 1074 to 1675) was reconstituted with different CLCs (48) and combined with the terminal-distal leg segment (TDD, residues 1 to 1074) (*SI Appendix*, Fig. S1E) under conditions promoting their coassembly (47). Cages produced when TDD was combined with CLC-reconstituted Hub fragments were similar in size to fragment cages without CLCs, and the larger cages observed for CLC variants associated with intact CHC did not form (Fig. 1 *D* and *E*). This result demonstrates that for CLC diversity to exert an effect on lattice curvature, the CHC knee must be intact, and shows that CLC splice variants differ in their influence on CHC knee conformation. Formation of larger cages by neuronal CLCs suggests that the neuronal splice inserts restrict the conformational flexibility of the CHC knee and could thereby reduce the likelihood of pentagon over hexagon formation. Nonneuronal CLCs appear to support a less biased variety of knee conformations, as cages of the two size classes are observed at almost equal frequency (Fig. 1 *B* and *C*). To establish whether cage size differences also correlated with CLC effects at the TxD, the different CLCs were compared for their ability to stabilize the TxD (*SI Appendix*, Fig. S2) in an assay that measures triskelion dissociation. While dissociation differences were observed between triskelia reconstituted with the different CLC isoforms and their splice variants, these effects did not correlate with cage size differences, suggesting that CLC influence at the vertex is not a major factor in lattice curvature.

CLC Diversity Modulates Mechanical Properties of the Clathrin Lattice.
We next investigated whether the influence of CLCs on the CHC knee had mechanical consequences for their ability to support membrane deformation. Mechanical properties of clathrin lattices were previously shown to be CLC-dependent and reduced ability of CLC-free clathrin to bend membranes in vitro was correlated with reduced planar lattice quality when assembled on an EM grid (21). To establish whether CLC diversity influences lattice quality in the same assay, clathrins with different CLC composition were assembled on EM grids coated with a clathrin-binding fragment of epsin1 (H_6-ΔENTH-epsin$^{144-575}$) (*SI Appendix*, Fig. S1F) (49). The flat lattices formed were visualized by EM and their periodicity (quality) assessed by Fourier transform analysis. Lattice quality was significantly reduced for clathrin with the neuronal splice variants nCLCa or nCLCb compared to clathrin reconstituted with their respective nonneuronal variants, and was significantly improved if formed from a 1:1 mix of nCLCa clathrin and nCLCb clathrin (Fig. 2). To visualize the nature of CLC distribution in these mixtures, lattices were generated using His-tagged nCLCa clathrin or nCLCb clathrin combined with the cognate untagged CLC and labeled with Ni-NTA-gold (*SI Appendix*, Fig. S3), confirming a uniform distribution of each neuronal CLC within the mixed lattice. In contrast to the behavior of the neuronal CLCs, lattice quality was reduced in mixtures of CLCa clathrin and CLCb clathrin compared to lattices formed by clathrin with only CLCa or CLCb.
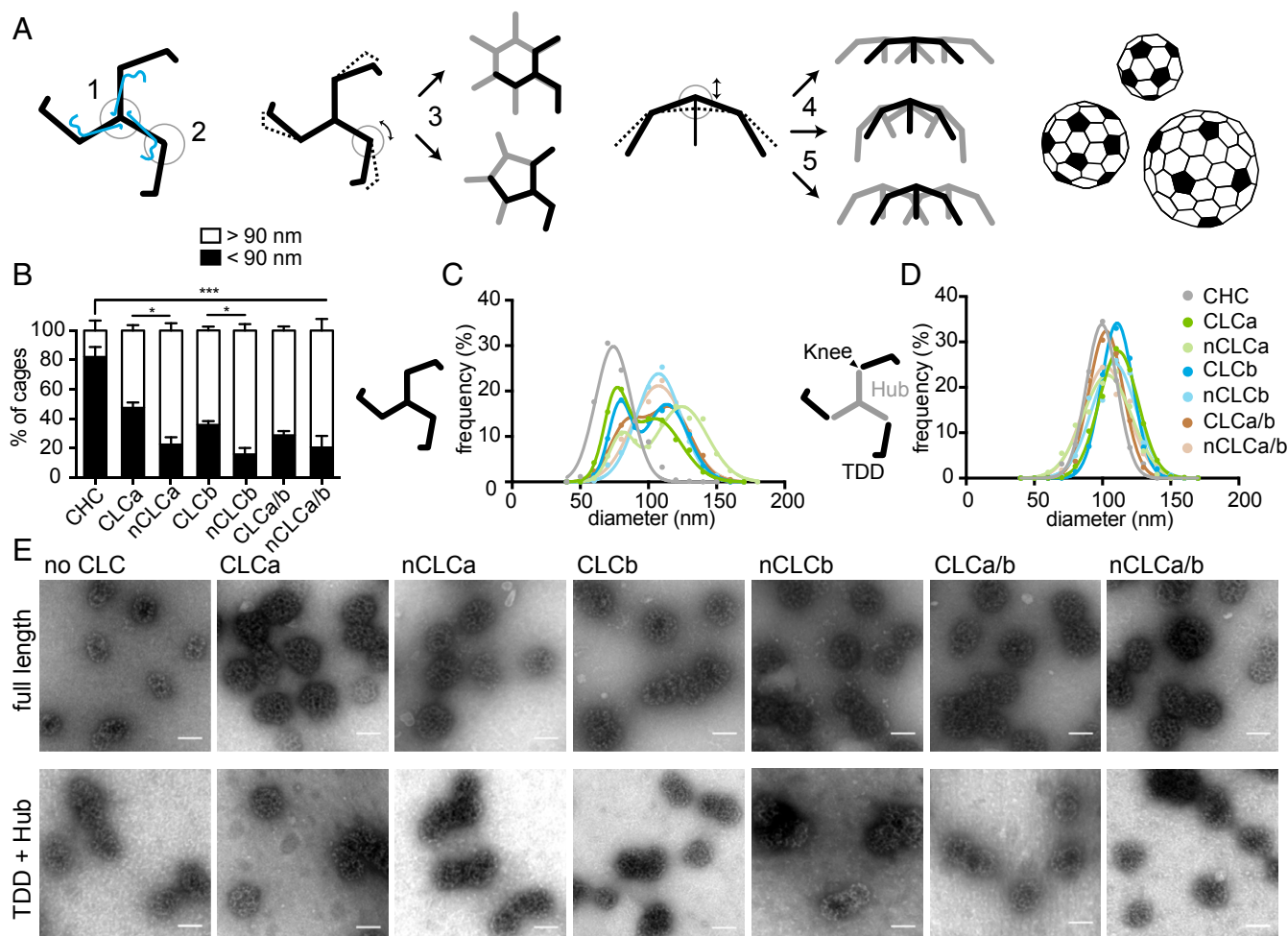
Fig. 1. CLCs differentially affect lattice curvature via regulation at the CHC knee. (*A*) Pucker (1) and knee (2) angles of the clathrin triskelion (black: CHC, blue: CLC) dictate lattice architecture. Different knee angles (encircled, black smooth and dashed lines) are adopted for hexagon (noncurvature inducing) or pentagon (curvature inducing) formation (3, whole triskelion in black and parts of others in gray). Lattice curvature is further amended through changes in pucker angle (4, dashed and black lines), or changes in proximal leg-crossing angle (5). CLC subunits are omitted for simplicity. Different sizes of closed cages are achieved by varying numbers of hexagons and a fixed number of 12 pentagons (filled black, based on ref. 45). (*B*) Quantification of the percentage of small cages (<90 nm in diameter) in a population of more than 200 cages, generated by in vitro assembly of clathrin reconstituted with indicated CLCs, 1:1 mixtures of reconstituted clathrins (CLCa/b or nCLCa/b), or CHC only (CHC), determined from electron micrographs (mean ± SEM, *P < 0.05, ***P < 0.001 one-way ANOVA followed by Holm–Sidak correction for multiple comparison, n = 3). (*C*) Cage size distributions from assemblies of triskelia formed from full-length CHC as described in *B*, with CLC composition key in *D*. (*D*) Size distributions of cages formed from TDD (black) and Hub (gray) coassemblies, with Hub fragments reconstituted or not with the indicated CLC isoforms or 1:1 mixtures of reconstituted Hubs. (*E*) Representative EM images of cages formed from full-length CHC (*Upper*) or Hub/TDD fragments (*Lower*) without or following reconstitution with indicated CLC isoforms. (Scale bars, 100 nm.)

To determine whether CLC-related variation in lattice quality correlated with membrane bending efficacy, as seen for complete absence of CLCs, we tested the function of the CLC-reconstituted clathrins using a low temperature in vitro budding assay (21). In this assay, H_6-ΔENTH-epsin$^{144−575}$, coupled to liposomes via modified Ni-NTA lipids, captures clathrin at the liposome surface. Lattice assembly on these liposomes can generate mature buds, which remain attached to the liposome due to lack of dynamin, needed for scission (21, 49). The efficiency of clathrin with different CLC composition to form such coated buds was assessed at 15 °C, a temperature permissive for budding by native clathrin but reduced for CLC-free clathrin (21). For each reconstituted clathrin, we measured the diameter of clathrin-coated membrane profiles in thin-section electron micrographs and assessed budding efficiency by the percentage of mature clathrin-coated buds (defined by a fitted diameter <200 nm) relative to the total clathrin-coated membrane observed including shallow pits and flat clathrin assemblies (defined by a fitted diameter >200 nm) (Fig. 3*A*). In line with previous findings, we found that at 15 °C native clathrin was about twice as effective in membrane deformation as CLC-free clathrin (21), and that budding efficiency varied with the CLC composition of clathrin tested (Fig. 3*B*). CLCa or CLCb clathrin lattices generated mature membrane buds more efficiently than clathrin with either single neuronal clathrin variant (Fig. 3 *B* and *C*), demonstrating that CLC splicing affects budding. Visualizing the clathrin-coated liposomes absorbed to EM grids confirmed that all clathrins tested assembled into intact lattices or buds on the liposome surface (*SI Appendix*, Fig. S4), suggesting that the observed variation in budding was not due to impaired lattice formation, but CLC-dependent lattice properties (21). Notably, mixing reconstituted neuronal clathrins significantly improved budding efficiency compared to clathrins with only one type of neuronal CLC (Fig. 3*D*), overall reflecting the same pattern as observed for both lattice quality and curvature (Table 1), suggesting all three parameters result from differential CLC effects at the triskelion knee. Furthermore, all three assays demonstrated
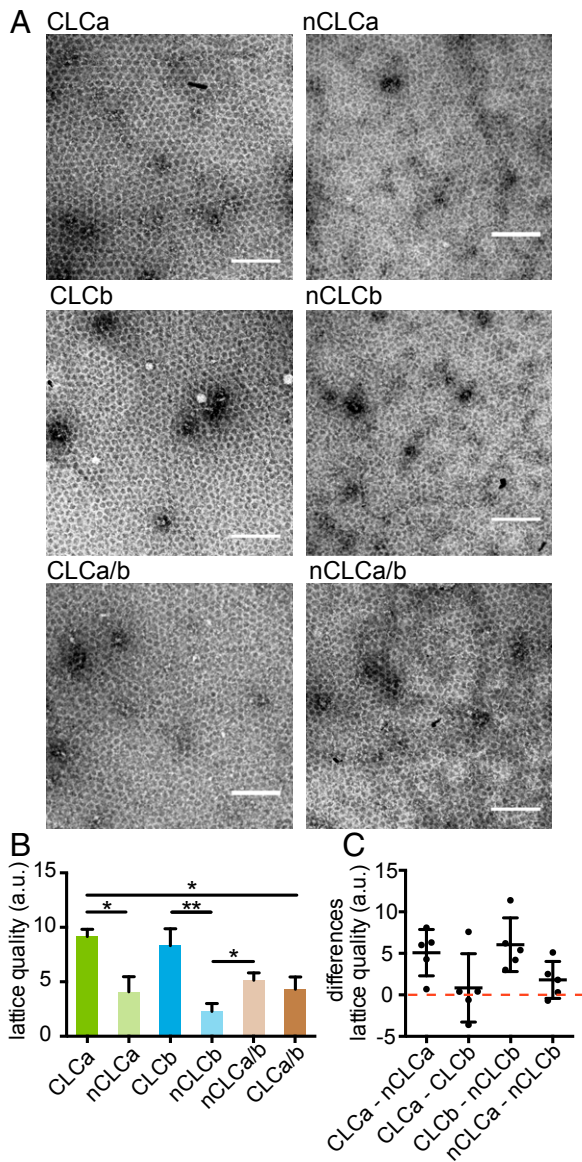
Fig. 2. CLC splicing and mixing affects in vitro lattice quality. (*A*) Clathrin reconstituted with indicated CLC isoforms and 1:1 mixtures of reconstituted clathrins were assembled into flat lattices and visualized by negative stain for EM analysis. (Scale bars, 200 nm.) (*B*) Quality (regularity quantified by Fourier transform) of lattices generated as in *A*, (mean ± SEM, *P < 0.05, **P < 0.01, one-way ANOVA followed by Holm–Sidak correction for multiple comparison, n = 5). (*C*) Differences in lattice quality between indicated reconstituted clathrins in individual experiments as in *B* (data points and mean ± SEM, n = 5).

that neuronal clathrin benefits from cooperative coassembly of clathrin with both isoforms.

Membrane deformation could result either from lattice formation at constant curvature or through transitioning from flat to curved lattices (Fig. 3*E*). Morphological analyses of clathrin-coated pits in human cell lines suggest that clathrin initially assembles into flat lattices at the plasma membrane and then gradually deforms the underlying membrane into coated buds (50, 51). To determine whether clathrin displayed these budding characteristics in our in vitro system and whether they are influenced by CLCs, we adopted the same EM-based approach. In micrographs of clathrin buds formed on liposomes, we measured the angle between the convex side of the coat and the coat-free membrane (Fig. 3*E*), coat curvature (i.e., diameter of the clathrin-coated structure), coat length and neck width for all coated membrane profiles (50), and then correlated these measurements. We observed a variety of coat curvatures (Fig. 3*F*) and found that neck width decreased with bud angle (Fig. 3*G*), as would be expected for both modes of deformation. Additionally, coat diameter correlated with the bud angle, characteristic of curvature transition (Fig. 3*H*), while we found no correlation between coat length and budding angle (Fig. 3*I*). Although this analysis is based on fixed structures at equilibrium, results were consistent with a flat to curved lattice transition, rather than assembly with constant curvature (Fig. 3 *H* and *I*). Thus, we conclude that budding in our in vitro system displays the same characteristics as observed in cells (50, 51), where curvature is most likely generated gradually through lattice rearrangement. Collectively, our results suggest that CLC splice variants and mixtures thereof differ in their ability to promote this transition and that this is due to variable restrictive influence on the flexibility of the triskelion knee within the lattice, which in turn affects clathrin's mechanical ability to deform membrane into coated buds (Table 1).

CLC Composition Affects SV Pool Size and Replenishment. Our in vitro experiments suggest that CLCs differentially affect clathrin's ability to deform membrane, with the neuronal isoforms working in conjunction for efficient membrane budding. Therefore, we predicted that neurons of animals with only one CLC isoform might be defective in clathrin-mediated pathways that contribute to SV formation. This hypothesis was investigated in knockout (KO) mice lacking the *Clta* or *Cltb* genes in all tissues (CLCa KO and CLCb KO mice). We previously generated CLCa KO mice (9) and have now produced CLCb KO mice. Loss of *Cltb* in CLCb KO mice was confirmed by PCR, and no CLCb or nCLCb protein was detected in all tissues analyzed (*SI Appendix,* Fig. S5). Whereas WT mice express a mixture of CLCs in most tissues (9), CLCa KO mice express only CLCb or nCLCb, and CLCb KO mice express only CLCa or nCLCa, enabling functional analysis of clathrin with only one type of CLC in neurons (Fig. 4*A*).

Hippocampal neurons have frequently been used to study the function of endocytic proteins in synaptic transmission (27, 30, 31, 33, 34, 52). H&E staining of the hippocampus showed no morphological abnormalities in either KO strain, indicating that absence of either CLC isoform does not affect gross hippocampus development in the CLC KO mice (*SI Appendix,* Fig. S6). We therefore analyzed the adult hippocampus in the CLC KO and WT mice to evaluate the function of mature excitatory synapses in the CA1 region, a region of well-defined neuronal architecture and neurophysiological circuitry. For electrophysiological recordings at Schaffer collateral (SC)-CA1 synapses in acute hippocampal slices, a stimulating electrode was placed in the SC fibers of the CA3 region and responses were then recorded in the CA1 pyramidal cell layer (Fig. 4*B*).

To determine the role of CLC diversity in SV pool replenishment in vivo, we recorded the responses to a prolonged high-frequency stimulus, which maximally depletes presynaptic terminals of the readily releasable pool (RRP) of SVs (53–55). Under these conditions, initial responses would draw from the preexisting SV pool, while sustained neurotransmission would rely on the efficiency of SV pool replenishment (54). Using this approach, we were able to assess CLC-dependency for different stages of SV exo- and endocytosis from these recordings. We found that the initial fusion efficiency of SVs in either KO strain was similar to that of their WT littermates, indicating that packaging of fusion-mediating cargo was not affected by changes in CLC composition (Fig. 4 *C* and *D* and *SI Appendix,* Fig. S7). Instead, both KO models had a decreased SV recycling rate
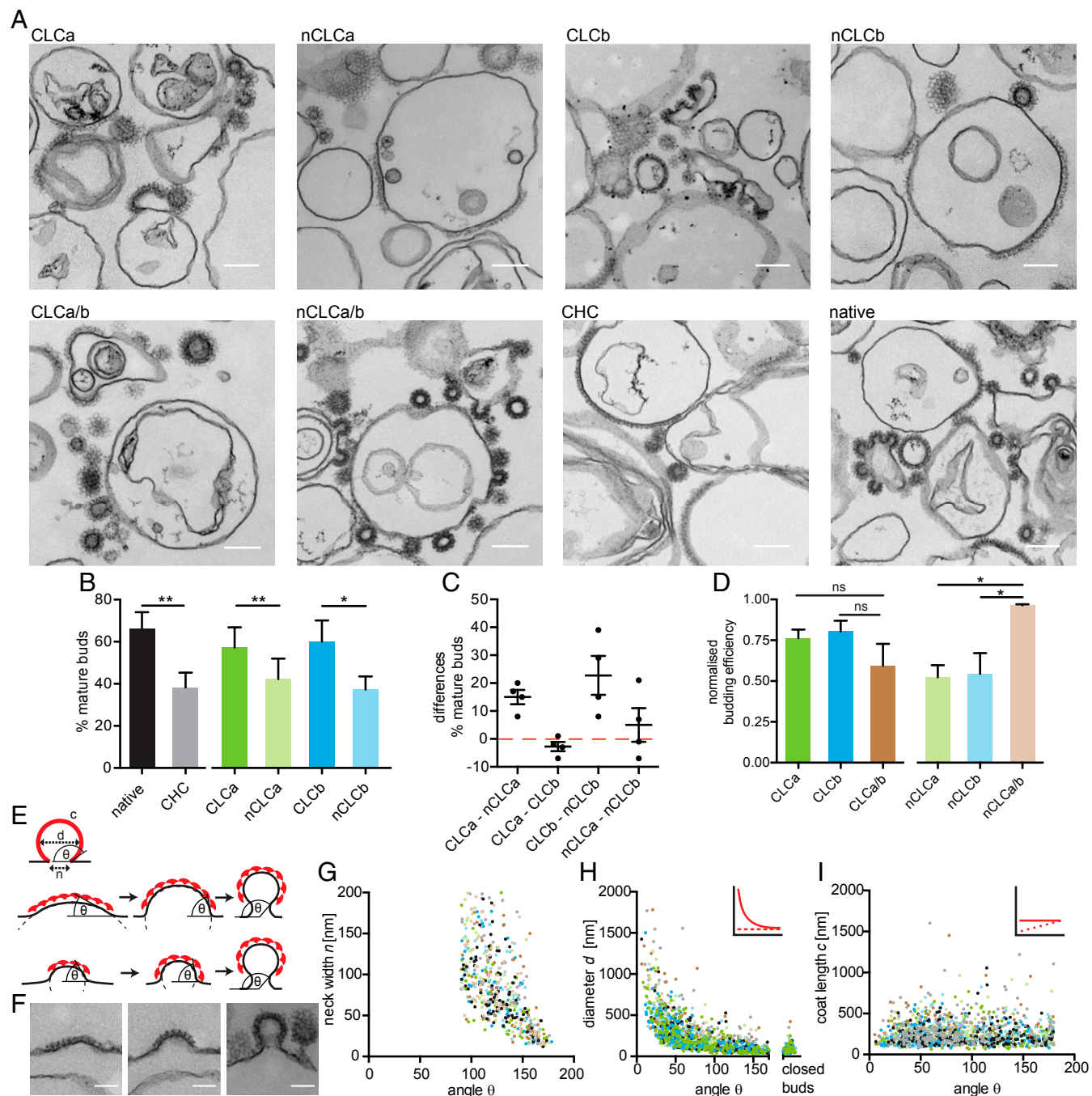
Fig. 3. CLC splicing and mixing affects in vitro lattice budding efficiency. (*A*) Representative EM images of clathrin reconstituted with indicated CLC isoforms, 1:1 mixtures of reconstituted clathrins, CHC only (CHC) and tissue-derived clathrin (native) assemblies on H_6-ΔENTH-epsin$^{144–575}$–coated liposomes. (Scale bars, 200 nm.) (*B*) Quantification of the percentage of mature buds (defined as clathrin-coated membrane profiles with <200 nm fitted diameter) of more than 60,000-nm total clathrin-coated membrane profiles including flat, shallow, and mature structures generated as in *A* (mean ± SEM, *P < 0.05, **P < 0.01, paired Student's *t* test for native and CHC, $n = 3$, one-way ANOVA with repeated measures for CLC-reconstituted clathrin, $n = 4$). (*C*) Differences in percentage of mature buds between indicated reconstituted clathrins in individual experiments in *B* (data points and mean ± SEM, $n = 4$). (*D*) Quantification of budding efficiency (percent mature buds determined as in *B*, normalized to native) of reconstituted clathrins and mixtures thereof (ns, not significant; *P < 0.05, one-way ANOVA for sets of neuronal or nonneuronal samples, followed by Holm–Sidak correction for multiple comparison, $n = 3$, $P = 0.052$, Student's *t* test for neuronal and nonneuronal mixtures, $n = 3$). (*E*) Parameters characterizing coated buds (*Top*); coat length *c*, membrane bud diameter *d*, neck width *n*, and budding angle θ. Models of clathrin-mediated membrane deformation by transitional curvature generation and lattice rearrangement (*Middle*), or lattice growth under constant lattice curvature (*Bottom*). (*F*) Representative coat profiles for flat (*Left*), shallow (*Center*), and mature budded (<200 nm fitted diameter, *Right*) structures. (Scale bars, 100 nm.) (*G–I*) Analysis of the dataset generated as shown in *A* for coated membrane parameters *n* (*G*), *d* (*H*), and *c* (*I*) as shown in *E* in relation to the θ of each structure measured for all reconstituted clathrins (colored as in *B* and *D*) within the same experiment. *Insets* in *H* and *I* show the different correlations of these parameters as predicted according to the curvature transition (red, smooth line) and constant curvature models (red, dashed line) shown in *E*.

Redlingshöfer et al.

Table 1. Regulation of clathrin lattice properties by CLC isoforms

	High					Low
Lattice curvature	CLCb	CLCa	nCLCa/b	CLCa/b	nCLCa	nCLCb
Lattice quality	CLCb	CLCa	nCLCa/b	CLCa/b	nCLCa	nCLCb
Budding efficiency	CLCb	CLCa	nCLCa/b	CLCa/b	nCLCa	nCLCb

characteristic of a defect in acute SV pool replenishment (Fig. 4 *C* and *D* and *SI Appendix*, Fig. S7). This finding correlated with our expectation from the in vitro studies that showed clathrin lattices with only one type of neuronal CLC were different from mixed lattices in their assembly properties (Table 1).

Further calculations based on data obtained from sustained trains of action potentials indicated that the RRP was larger in the CLCb KO mice but reduced in the CLCa KO mice when compared to WT littermates (Fig. 4 *C* and *D* and *SI Appendix*, Fig. S7), revealing a phenotype that we did not expect from our in vitro data. To establish whether the SV formation was altered in the CLC KO mice rather than the ability to mobilize SVs from other SV pools, we assessed the ultrastructure of excitatory synapses in the CLC KO mice and their WT littermates (Fig. 4*E*). Indeed, SV density was significantly reduced in hippocampal neurons in the CLCa KO animals. In contrast, SV density in equivalent neurons of the CLCb KO mice was significantly increased compared to their WT littermates (Fig. 4 *F* and *J*), in line with our RRP estimates from electrophysiological recordings (Fig. 4 *C* and *D*). Other parameters, such as individual SV size (Fig. 4 *G* and *K*), postsynaptic density length (Fig. 4 *H* and *L*), and excitatory synapse density (Fig. 4 *I* and *M*) were similar between both KO strains and respective WT littermates. Together, these data show that CLCs are required for efficient and sustained synaptic function and suggest that loss of either CLC decreases acute SV replenishment by affecting immediate formation, correlating with expectations from reduced in vitro budding efficiency, but that the KO strains differ in their ability to generally maintain SV pools. Thus, CLC composition influences SV density in excitatory neurons of the hippocampus, and nCLCa and nCLCb function differently in SV generation such that mice with only nCLCa can sustain a compensatory pathway for SV generation and mice with only nCLCb cannot.

CLCa KO and CLCb KO Mice Have Distinct Neurological and Behavioral Defects. To further investigate the differential consequences of CLCa or CLCb KO for synapse function, we conducted additional electrophysiological experiments to characterize synaptic transmission in our KO animals. Analyses of the evoked excitatory postsynaptic current (EPSC) responses to stimuli of increasing magnitude revealed decreased EPSC response amplitude in the CLCa KO mice compared to WT littermates, suggesting impaired basal synaptic transmission in the CLCa KO mice (Fig. 5*A*). In contrast, the evoked EPSC response amplitude in hippocampal slices from the CLCb KO mice was of similar or higher magnitude than that of their WT littermates, suggesting that basal synaptic transmission was intact or even enhanced (Fig. 5*B*). These differences in synaptic connectivity between hippocampal function in the two KO strains could arise from defects in presynaptic neurotransmitter release correlating with differences in SV pool size in the KO animals relative to their WT littermates (Fig. 4).

We then performed paired-pulse ratio (PPR) recording experiments, an approach that allows assessment of defects in neurotransmitter release (56, 57). In excitatory neurons such as those analyzed here, a second stimulus pulse (P_2) fired in short succession after an initial pulse (P_1) results in a larger response

than the first stimulus. This facilitation is dependent on changes in the probability of neurotransmitter release. PPR is inversely correlated with release probability, as a lower initial release probability leaves more vesicles remaining at the terminal, which are then capable of being released after the second stimulus (56, 57). We observed that, compared to WT littermates, the PPR was increased in CLCa KO mice, consistent with a reduction in release probability (Fig. 5*C*). In contrast, no differences in PPR were observed in CLCb KO mice compared to WT littermates (Fig. 5*D*). Thus, specific loss of nCLCa impairs presynaptic function compromising neurotransmitter release at the SC-CA1 synapse. Collectively, our electrophysiological data support the morphological data (Fig. 4 *E–M*), indicating that neurons with only nCLCa clathrin can compensate for defective SV regeneration by expanding their SV pool from another pathway, while neurons with only nCLCb clathrin cannot compensate and show diminished SV pools from impaired replenishment.

Ongoing breeding of the CLCa KO colony confirmed a 50% survival rate compared to that expected for homozygous CLCa KO mice (9), whereas homozygous CLCb KO mice had no survival defects (Fig. 5*E*). Survival phenotypes similar to the CLCa KO animals have been reported for other genetic deletions in endocytic pathways, which also displayed neuronal phenotypes (30) in the hippocampus and other regions of the brain (32). Therefore, we assessed performance in the rotarod test for neuro-motor coordination for both CLC KO mice (58). Compared to their WT littermates, surviving CLCa KO mice displayed defects in rotarod balance, whereas CLCb KO mice did not (Fig. 5*F*). Further assessment of sensorimotor function revealed that CLCa KO mice exhibited defects in a grid-walking test (Fig. 5*G*), but not in grip strength (Fig. 5*H*), suggesting neurological rather than muscular dysfunction in the CLCa KO animals, supporting the notion that loss of nCLCa is less tolerable than loss of nCLCb. Together, the phenotypes of the KO animals indicate that neuronal CLC isoforms are differentially able to support compensatory mechanisms for adjusting SV pool size in hippocampal synapses with impaired acute SV replenishment, and suggest that clathrin with only nCLCa enables more functions than clathrin with only nCLCb, while a mix of both neuronal CLCs is necessary for optimal clathrin function in neurons, consistent with their synergistic contribution to clathrin function in vitro.

Discussion

To understand the consequences of CLC diversity for clathrin function, we characterized the biophysical properties of in vitro assemblies formed from clathrin comprising single CLC isoforms and correlated these properties with neuronal phenotypes observed in KO animals expressing single CLC isoforms. We found that neuronal CLC splicing affects lattice properties (Figs. 1*B* and 2*B*) by diversifying the CLC influence on the CHC knee to regulate lattice curvature (Fig. 1 *C* and *D*) and deform membrane (Fig. 3*B*). Our in vitro studies further suggest that lattices formed from mixtures of clathrin with nCLCa and nCLCb have different assembly properties and are more efficient in membrane deformation compared to clathrin with only one type of neuronal CLC (Figs. 2*B* and 3*D*). Consistent with this observation, neurons from both CLCa and CLCb KO mice showed
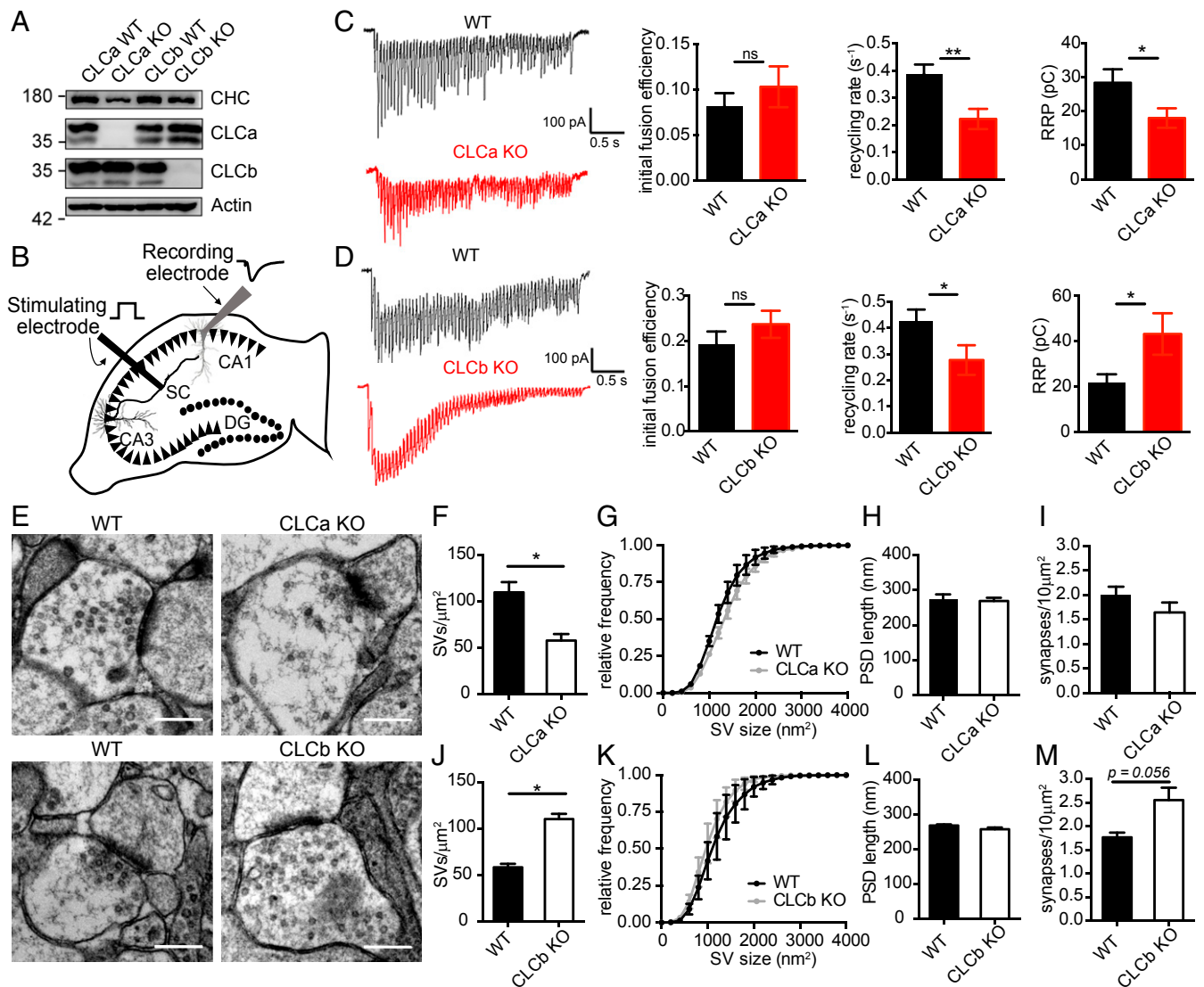
Fig. 4. CLC composition regulates SV pool replenishment in hippocampal neurons. (*A*) Immunoblot of CLC KO and WT brain lysate for CHC (TD.1 antibody), CLCa (X16 antibody), CLCb (CLTB antibody), and actin (anti–β-actin antibody). (*B*) Schematic illustration of stimulating and recording electrode set-up in acute hippocampal slices. The synapses investigated are formed by a Schaffer collateral (SC) axon (black) from a pyramidal neuron (black triangles, cell bodies) in the CA3 region synapsing with a receiving pyramidal neuron (gray triangle, cell body) in the CA1 region from which responses are recorded. Black circles denote dentate gyrus (DG) granule cell bodies. (*C*) Representative traces of evoked EPSCs following a 20-Hz electrical stimulation for 3 s in CLCa KO and WT hippocampal slices (*Left*). Graphs (*Right*) show the mean (± SEM) initial fusion efficiency, SV recycling rate, and RRP size calculated for all cells (*n* = 9 to 11 cells from 3 animals per genotype; *$P < 0.05$ and **$P < 0.01$, unpaired Student's *t* test). (*D*) Representative traces of EPSCs following a 20-Hz electrical stimulation for 3 s in CLCb KO and WT hippocampus slices (*Left*). Graphs (*Right*) show the mean (± SEM) initial fusion efficiency, SV recycling rate and RRP size calculated for all cells (*n* = 11 to 12 cells from 4 animals per genotype; *$P < 0.05$, unpaired Student's *t* test). (*E*) Representative EM images of excitatory synapses in the CA1 region of the hippocampus of CLCa WT, CLCa KO, CLCb WT, and CLCb KO. (Scale bars, 300 nm.) (*F–M*) Quantification of data extracted from EM images as in *E*. Graphs show SV density within 300 nm of the postsynaptic density (PSD) (*F* and *J*), cumulative frequency distribution of SV size (*G* and *K*), PSD length (*H* and *L*), and synapse density (*I* and *M*) expressed as mean ± SEM (*$P < 0.05$, unpaired Student's *t* test, *n* = 3).

defects in synaptic transmission that indicated acute clathrin-dependent SV replenishment was impaired (Fig. 4 *C* and *D*). However, the CLCa KO mice had reduced numbers of SVs in their hippocampal synapses, while the CLCb KO mice had more SVs than their WT littermates (Fig. 4 *F* and *J*). Thus, although acute SV replenishment was impaired in both KO strains, clathrin with only nCLCa (in the CLCb KO mice) was able to support a compensatory pathway of SV formation, while clathrin with only nCLCb (in the CLCa KO) was not (Fig. 5 *A–D*). These findings establish functional differences between CLC isoforms in vitro and in vivo and demonstrate how resulting clathrin diversity, as well as CLC isoform balance, are important for clathrin function in neurons.

Neuronal splicing predominates for CLCb in neurons (59), while neuronal CLCs are not present in other brain cells, such as glial or Schwann cells (20), indicating that the CLC splice variants segregate within brain cell types to fulfill distinct functions. Neuronal CLC variation due to splicing had a significant influence on lattice curvature and budding efficiency. Compared to clathrin with nonneuronal CLCs, clathrin with neuronal CLCs formed predominantly large cages in solution (with low a pentagon-to-hexagon ratio), suggesting that through their influence on the CHC knee (Fig. 1*D*), the spliced inserts reduce triskelion flexibility to accommodate pentagonal faces. When constrained to a flat, solid surface (EM grid), lattice assembly requires significant deformation of triskelia (21). The quality of
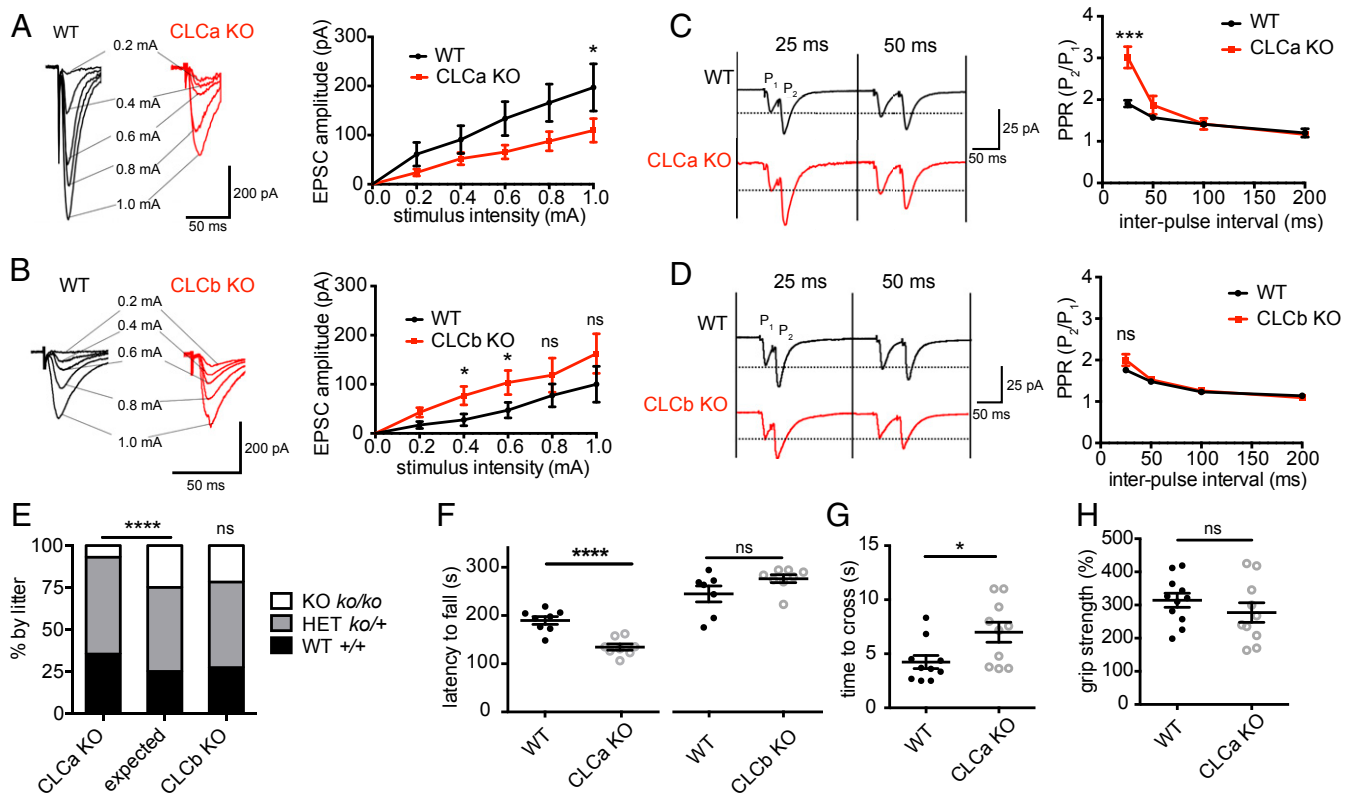
Fig. 5. Neuronal defects are compensated for in CLCb KO but not CLCa KO mice. (*A*) Input–output relationship of evoked EPSCs at CA1 synapses of WT and CLCa KO hippocampus slices. Traces show responses of representative cells at increasing stimulus intensity with an average of three responses for each stimulus strength (mean ± SEM; n = 9 to 11 cells from 3 animals per genotype; *$P < 0.05$, two-way ANOVA with repeated measures). (*B*) Input–output relationship of evoked EPSCs at CA1 synapses of WT and CLCb KO hippocampus slices. Traces show response of representative cells at increasing stimulus intensity with an average of three responses for each stimulus strength (mean ± SEM; n = 12 to 15 cells from 4 animals per genotype; *$P < 0.05$, two-way ANOVA with repeated measures). (*C*) PPR of evoked EPSCs at CA1 synapses of WT and CLCa KO hippocampal slices. Traces show responses of representative cells. Graph displays the mean PPR (P_2/P_1 ± SEM) from all cells (n = 9 to 11 cells from 3 animals per genotype) at different time intervals between paired pulses (***$P < 0.001$, unpaired Student's t test). (*D*) PPR of EPSCs at CA1 synapses of WT and CLCb KO hippocampal slices. Traces show responses of representative cells. Graph displays the mean PPR (P_2/P_1 ± SEM) from all cells (n = 12 to 15 cells from 4 animals per genotype) at different time intervals between paired pulses. (*E*) Genotype distribution for CLCa KO (n = 590) and CLCb KO (n = 359) mice after weaning compared to expected distribution (****$P < 0.0001$, χ^2 test). (*F*) Performance in the accelerated rotarod test (latency to fall) by CLC KO (CLCa KO = 8, CLCb KO = 8) and control WT littermates (CLCa WT = 8, CLCb WT = 7) expressed as data points and mean ± SEM (****$P < 0.0001$, unpaired Student's t test). (*G*) Time to cross grid for CLCa KO (n = 10) and control mice (n = 10) expressed as data points and mean ± SEM (*$P < 0.05$, unpaired Student's t test). (*H*) Grip strength of CLCa KO (n = 10) and control mice (n = 11, gram-force relative grip strength over body weight) expressed as data points and mean ± SEM.

lattices formed by clathrin with neuronal CLCs under these conditions was reduced compared to clathrin with nonneuronal CLCs, further suggesting that neuronal CLCs restrict clathrin's conformational flexibility. Notably, CLC-dependent lattice quality and cage size correlated with the ability of clathrin with different CLCs to produce mature buds at liposome membranes, which morphological analysis suggested are generated by flat lattice rearrangement, as observed at cell membranes (50, 51). Together, these results suggest that CLC splicing variation influences clathrin's flexibility to form and alternate between a range of morphologies in order to deform lipid membrane into mature clathrin-coated buds, and that this is attributable to CLC influence on the CHC knee domain.

Given that the inserted sequences are located near the TxD where the C termini of CLCs are bound (arrowheads, Fig. 6*A*), we propose that the splice inserts affect the conformation of the adjacent knee of a neighboring triskelion, which is closer to the inserted sequences than the knee of the triskelion to which the CLC is bound (Fig. 6*B*). This intermolecular influence could involve splice inserts at the C terminus (stars, Fig. 6*B*) interacting with the neighboring CHC knee or with the N-terminal domain (N) of a CLC bound to the neighboring knee (Fig. 6*B*).

Considering the average 40% sequence differences between CLCa and CLCb isoforms and their even greater variation at the N terminus, inter-CLC interactions could vary depending on which splice isoform interacts with which CLC isoform N terminus, thereby influencing overall lattice properties. This potential interaction may be lost from clathrin with nonneuronal CLCs, which would explain why mixing nonneuronal CLC isoforms does not affect in vitro membrane deformation to the same extent as mixing neuronal CLC isoforms (Fig. 3*D*).

Here, we characterize the properties of homo- and heteroassemblies of clathrin comprising single CLC isoforms. In the brain, CLC isoforms are apparently randomly distributed on triskelia (60), in which case neuronal inserted sequences could still influence lattice curvature via interactions with an adjacent triskelion knee. The presence of nCLCb would serve as an attenuator of nCLCa-specific interactions and vice versa. Furthermore, in cells where CLCb expression is transiently increased (61), newly synthesized triskelia would be generally occupied by a single CLC isoform, as clathrin subunit turnover is slow (62). The resulting homotypic clathrins would then participate mixed in lattices, as we have studied here. Thus, neuronal CLC isoform expression ratios (and/or local abundance within
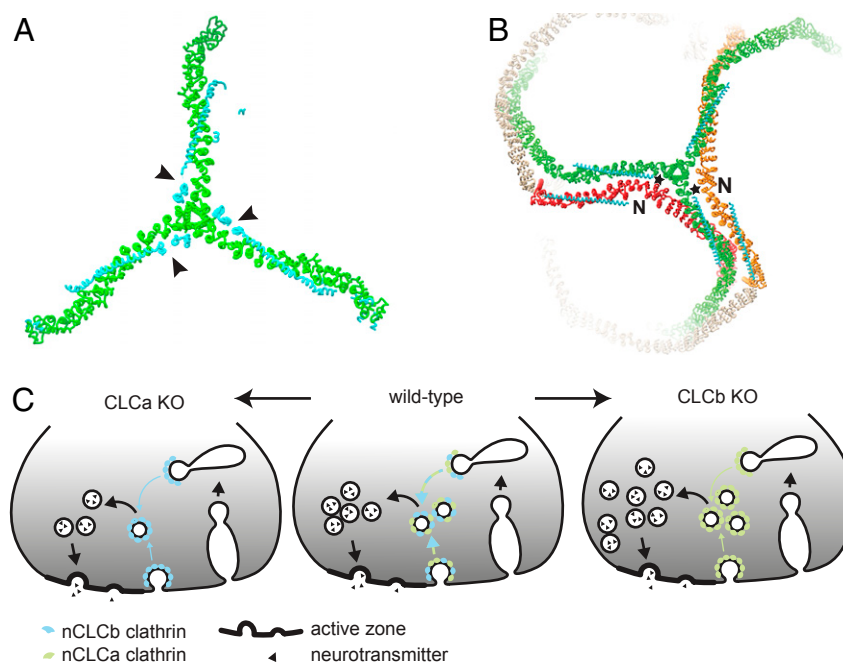
Fig. 6. Model of how neuronal CLC diversity regulates SV recycling and lattice properties. (*A*) CLC (cyan) neuronal splice inserts (arrowheads) are located near the TxD of the bound CHC (green, left, PDB ID code 3LVH). (*B*) CLC (cyan) neuronal splice inserts (stars) are near the CHC knee of the neighboring triskelion (red or orange) within lattices (right, PDB ID code 3IYV). Interaction between a neuronal splicing insert and the knee of an adjacent triskelion and/or adjacent CLC N terminus (N) could promote conformational change in the CHC knee. As the formation of pentagons and hexagons requires different knee angles, this interaction could consequently influence lattice curvature (see Fig. 1*A*). (*C*) In WT mice (*Center*), a mix of nCLCa and nCLCb clathrin creates the appropriate biophysical properties to mediate SV generation from endosomal compartments (and possibly the plasma membrane, blue-green arrows). Loss of nCLCa (*Left*) creates nCLCb clathrin lattices that are defective in efficient SV regeneration (blue arrows), resulting in decimated SV pools. Loss of nCLCb (*Right*) creates nCLCa clathrin lattices, which are also less efficient in SV regeneration than WT, but able to maintain an overall increased SV pool by excess budding to compensate for reduced efficiency in acute SV pool replenishment (green arrows).

cells) could tailor clathrin lattice properties specifically to particular needs.

There are several pathways involved in SV recycling in neurons and the role of clathrin has been widely debated, possibly because the contribution of each pathway to SV formation is variable between organisms, types of neurons, and stimulus (52, 63, 64). SV recycling can either be achieved by direct regeneration of SVs through clathrin-mediated endocytosis from the plasma membrane at low-frequency stimulus, or through clathrin-independent mechanisms, which predominantly mediate retrieval of SV components from the plasma membrane under high stimulus (2, 27, 28, 33, 52). Rapid clathrin-dependent trafficking of SV proteins from the endosomal pathway then leads to resorting and formation of SVs at high-frequency stimulus (2), which can occur in a timeframe of 1 to 3 s after stimulation (27). In our analysis of neurotransmission, SV recycling defects were detected by electrophysiology within 3 s at high stimulus (20 Hz for 3 s), suggesting the defects detected were due to impaired clathrin-mediated regeneration of SVs from the endosomal pathway. These findings are consistent with previously observed roles for CLCs in recycling from nonneuronal endosomal compartments (61, 65).

That neurons in both CLC KO strains shared an acute defect in SV pool replenishment fits with our in vitro biophysical data that demonstrate single neuronal CLCs are not as efficient in membrane deformation as a mixture of clathrin with both neuronal CLCs (Fig. 3*D*). In response to this defect, we found that clathrin with only nCLCa generated an increased steady-state SV pool in CLCb KO neurons, while clathrin with only nCLCb could not (Fig. 4). CLCa seems to have preferential connection with the actin cytoskeleton compared to CLCb (12, 14), which might account for the ability of nCLCa clathrin to function on its own

without nCLCb and benefit from involvement of actin and its accessory molecules in this compensatory pathway. It is possible that in the (normal) presence of nCLCb, the actin interactions of nCLCA may be "diluted down," so that nCLCb works as an attenuating balancing mechanism to control SV pools at steady state. The presence of nCLCb would simultaneously create lattice properties for efficient CCV budding during neurotransmission. In its absence, the acute replenishment pathway would decrease in efficiency but loss of the nCLCb attenuation effect enables a compensatory pathway with nCLCa only (Fig. 6*C*). Thus, the budding defect resulting from a change in biophysical properties of clathrin is detectable only under acute demand, and when demand is less acute, there are mechanisms by which nCLCa clathrin can generate SVs that are not supported by nCLCb clathrin.

Considering the whole animal phenotypes, including the increased mortality rate for CLCa but not CLCb KO animals, CLCa seems able to sustain housekeeping clathrin functions, while CLCb functions mainly in conjunction with CLCa, apparently in a regulatory capacity, such that a balance between the two is required for some specialized functions. This is in line with the observation that CLC expression ratios vary with tissue, and while lymphoid cells almost exclusively express CLCa, no tissue has been found to express exclusively CLCb (9, 62). CLC isoform splicing changes during cell differentiation, development (10, 59), and ratios of CLCb relative to CLCa are modulated in tumor progression (13) and cell migration (61). These observations, in combination with the in vitro and in vivo data reported here, support the concept that, in addition to influencing accessory protein interaction, the conserved vertebrate CLC isoform and splicing differences facilitate tissue-specific clathrin functions by directly modulating clathrin lattice properties. In

BIOCHEMISTRY

particular, CLC diversity regulates clathrin budding efficiency, a property that we show here affects SV formation under acute demand, and is likely to influence other pathways that rely on rapid clathrin-mediated membrane traffic.

Materials and Methods

Protein Expression and Purification. Except for full-length CHC, all proteins were recombinantly expressed in bacteria and purified by standard affinity and size-exclusion chromatography methods, as specified in *SI Appendix, Supplementary Methods*. Native clathrin and full-length CHC were prepared from porcine brain as specified in *SI Appendix, Supplementary Methods*.

Characterization of Clathrin Lattice Properties. For lattice curvature determination, cage assembly was induced by dialysis in assembly-promoting buffer A (100 mM MES pH 6.4, 1 mM EGTA, 0.5 mM MgCl$_2$, 2 mM CaCl$_2$) and cage size distributions analyzed from EM images, as specified in *SI Appendix, Supplementary Methods*. Flat lattices were produced and analyzed as previously described (21) and as detailed in *SI Appendix, Supplementary Methods*. Lattice regularity was assessed from electron micrographs of similar quality and various focuses for each specimen as a measure of lattice quality. Five to 12 images were analyzed for each reconstituted clathrin isoform within each of three independent sets of experiments. In vitro budding was performed as previously described (49). In brief, H$_6$-ΔENTH-epsin$^{144-575}$ was bound to liposomes made from brain polar lipid extracts containing 5% DGS-Ni-NTA lipids (Avanti). H$_6$-ΔENTH-epsin$^{144-575}$–coated liposomes were then chilled to 15 °C and mixed with clathrin triskelia at 15 °C, incubated for 30 min at 15 °C and then transferred to ice. Samples were then fixed at 4 °C overnight and processed for EM analysis. Diameter, coat length, bud angle, and neck width of clathrin-coated membrane profiles were measured from electron micrographs using ImageJ (NIH) and data processed using Prism (GraphPad). Between 150 and 200 coat profiles, randomly sampled across four thin sections, were analyzed for each sample (>60,000-nm total coat length per experiment per sample). The proportion of mature buds, defined by a diameter of less than 200 nm, of all clathrin-coated membrane profiles examined, was used as a measure of budding efficiency. Results from three to five independent sets of experiments were tested for statistical significance.

Generation of CLC KO Mice. The *Cltb*$^{ko/ko}$ mouse strain was created from embryonic stem (ES) cell clone 19159A-F4, generated by Regeneron Pharmaceuticals, and obtained from the KOMP Repository (https://www.komp.org/). Methods used to create the CLCb-null ES cell clone have previously been published (66). In brief, the complete coding region of the *Cltb* gene was fully deleted by homologous recombination using a large BAC-based targeting vector. Targeted ES cells were then injected into albino C57BL/6J-N blastocytes and transferred into foster mothers. Chimeric offspring were mated with C57BL/6J females (Charles River), and germline transmission of the *Cltb*-null allele (*Cltb*^{ko}) was established. Heterozygote *Cltb*$^{ko/+}$ mice were backcrossed on the C57BL/6 background and bred to produce *Cltb*$^{ko/ko}$ homozygous mice. CLCa KO mice (C57BL/6 background) (9) were produced by breeding *Clta*$^{ko/+}$ heterozygotes. WT littermates from the same breedings were used as controls for homozygous KO animals. All procedures involving animals were conducted according to the Animals Scientific Procedures Act UK (1986) and in compliance with the ethical standards at University College London.

Analysis of Protein Expression in Brain. Mouse brains were harvested from six 9- to 12-mo-old C57BL/6 WT and homozygous CLCa and CLCb KO mice and snap-frozen in liquid nitrogen and stored at −80 °C until further use. Tissue were quickly thawed and homogenized in lysis buffer (50 mM Hepes pH 8.0, 50 mM NaCl, 1% Triton-X 100, 5 mM EDTA, 2 mM CaCl$_2$, 1 mM PMSF, cOmplete Protease Inhibitor Mixture [Roche]). The homogenate was further incubated on ice for 45 min before centrifugation at 21,000 × *g* and 4 °C for 2 × 10 min in an Eppendorf 5424 R benchtop centrifuge (Eppendorf). Protein content of the lysate was determined by BCA assay (Thermo Fisher). For analysis, 25 μg of sample was loaded on 4 to 15% acrylamide gels (Bio-Rad) and subjected to SDS/PAGE and immunoblotting. Primary antibodies used for immunoblotting were TD.1 (anti-CHC, made in-house) (67), X16 (anti-CLCa, made in-house) (68), CLTB (anti-CLCb, Proteintech), and anti–β-actin (Sigma-Aldrich).

Electrophysiology. Experiments were performed in 8- to 10-mo-old mice. Both male and female mice were used for electrophysiological experiments. Acute transverse hippocampal slices (300 μm) of homozygous CLCa or CLCb KO and control mice were cut on a Leica VT-1000 vibratome in ice-cold artificial cerebrospinal fluid (ACSF) bubbled with 95% O$_2$/5% CO$_2$ containing: NaCl (125 mM), KCl (2.4 mM), NaHCO$_3$ (26 mM), NaH$_2$PO$_4$ (1.4 mM), D-(+)-Glucose (20 mM), CaCl$_2$ (0.5 mM) and MgCl$_2$ (3 mM). At 5-min intervals, slices were then transferred into a series of three different chambers oxygenated (95% O$_2$/5% CO$_2$) in the same base ACSF but with the following temperature and component variations: 1) 21 °C initially with MgCl$_2$ (1 mM) and CaCl$_2$ (0.5 mM) then allowed to heat gradually to 36 °C; 2) 36 °C with MgCl$_2$ (1 mM) and CaCl$_2$ (1 mM); and 3) 36 °C initially with MgCl$_2$ (1 mM) and CaCl$_2$ (2 mM) before cooling to 21 °C. Slices were then left for at least 1 h before recordings commenced.

Evoked recordings were performed on an upright microscope continually perfused with oxygenated recording solution at room temperature containing the same ACSF composition as the third chamber and supplemented with 10 μM bicuculline. Pyramidal cells in the CA1 region were held at −60 mV in whole-cell voltage-clamp configuration using glass microelectrodes (resistance 3 to 8 MΩ) filled with caesium gluconate intracellular solution containing: D-gluconic acid lactone (130 mM), Hepes (10 mM), EGTA (10 mM), NaCl (10 mM), CaCl$_2$ (0.5 mM), MgCl$_2$ (1 mM), ATP (1 mM) and GTP (0.5 mM), QX314 (5 mM), pH to 7.2 with CsOH. To evoke postsynaptic EPSCs, a bipolar concentric stimulation electrode (FHC) was placed in the SC fibers of the CA3 region. For input–output recordings, the stimulus pulse was varied between 0.2 and 1 mA with a pulse width of 0.1 ms and stimuli were delivered at a rate of 0.1 Hz. Paired pulse stimuli were given at rate of 0.2 Hz with different interstimulus intervals, ranging from 25 ms to 200 ms and a stimulation strength set to ~50% of the maximal response for each cell. PPR was calculated as the ratio of the peak amplitude of the second response over the first response. Calculation of RRP size, initial fusion efficiency, and SV recycling rate was done on ESPC recordings that underwent 3 s duration trains of stimulation at 20 Hz and estimated as previously described (54, 69). Briefly, RRP size, fusion efficiency (*fe*), and vesicle recycling rate (α) were evaluated from the cumulative charge during the stimulation train using the following two equations:

$$fe = \frac{r(1)}{r(\infty)}(1 - \exp(-\alpha\Delta t)) \qquad [1]$$

$$fe = \frac{r(1)}{\sum_{i=1}^{s} r(i)\exp(-\alpha(S-i)\Delta t)} \qquad [2]$$

where $r(1)$ is the charge of the first EPSC in the train, $r(i)$ the charge passed by the *i*th EPSC, $r(\infty)$ was calculated from the average charge of the last 10 EPSCs in the train, and Δt is the stimulus interval in the train. The RRP was estimated as RRP = $r(1)/fe$.

All currents were recorded using an Axopatch 200B amplifier, filtered (1 kHz), and digitized (10 kHz). Data were monitored online and analyzed offline using WinEDR and WinWCP software (available free online at http://spider.science.strath.ac.uk/sipbs/software_ses.htm). Stimulus artifacts in representative traces were digitally removed for clarity.

Statistical Analysis. All experiments were performed at least three times. All calculations and graphs were performed with ImageJ, Microsoft Excel, and GraphPad Prism software. *P* values were calculated using two-tailed Student's unpaired or paired (in vitro budding) *t* tests, two-way ANOVA with repeated measures (electrophysiology), one-way ANOVA followed by Holm–Sidak correction for multiple comparison or one-way ANOVA for preselected pairs without correction for multiple comparison (clathrin biophysical properties). Detailed statistical information including statistical tests used, number of independent experiments, *P* values, and definition of error bars is described in the individual figure legends.

Additional Methods. Details on methods for protein purification and assays, mouse genotyping and behavioral tests, EM, and ultrastructure analysis are in *SI Appendix, Supplemental Methods*.

Data Availability. All data generated and protocols used in this study are included in the main text and *SI Appendix*. Requests for materials and animals described should be addressed to F.M.B.

1. F. M. Brodsky, Diversity of clathrin function: New tricks for an old protein. *Annu. Rev. Cell Dev. Biol.* **28**, 309–336 (2012).
2. T. Soykan, T. Maritzen, V. Haucke, Modes and mechanisms of synaptic vesicle recycling. *Curr. Opin. Neurobiol.* **39**, 17–23 (2016).
3. H. T. McMahon, E. Boucrot, Molecular mechanism and physiological functions of clathrin-mediated endocytosis. *Nat. Rev. Mol. Cell Biol.* **12**, 517–533 (2011).
4. P. N. Dannhauser et al., CHC22 and CHC17 clathrins have distinct biochemical properties and display differential regulation and function. *J. Biol. Chem.* **292**, 20834–20844 (2017).
5. A. P. Jackson, H. F. Seow, N. Holmes, K. Drickamer, P. Parham, Clathrin light chains contain brain-specific insertion sequences and a region of homology with intermediate filaments. *Nature* **326**, 154–159 (1987).
6. T. Kirchhausen et al., Clathrin light chains LCA and LCB are similar, polymorphic, and share repeated heptad motifs. *Science* **236**, 320–324 (1987).
7. D. E. Wakeham et al., Clathrin heavy and light chain isoforms originated by independent mechanisms of gene duplication during chordate evolution. *Proc. Natl. Acad. Sci. U.S.A.* **102**, 7209–7214 (2005).
8. M. Fumagalli et al., Genetic diversity of CHC22 clathrin impacts its function in glucose metabolism. *eLife* **8**, e41517 (2019).
9. S. Wu et al., Clathrin light chains' role in selective endocytosis influences antibody isotype switching. *Proc. Natl. Acad. Sci. U.S.A.* **113**, 9816–9821 (2016).
10. J. Giudice et al., Alternative splicing regulates vesicular trafficking genes in cardiomyocytes during postnatal heart development. *Nat. Commun.* **5**, 3603 (2014).
11. M. Mettlen et al., Endocytic accessory proteins are functionally distinguished by their differential effects on the maturation of clathrin-coated pits. *Mol. Biol. Cell* **20**, 3251–3260 (2009).
12. O. M. Tsyankova, J. H. Keen, A unique role for clathrin light chain A in cell spreading and migration. *J. Cell Sci.* **132**, jcs224030 (2019).
13. P. H. Chen et al., Crosstalk between CLCb/Dyn1-mediated adaptive clathrin-mediated endocytosis and epidermal growth factor receptor signaling increases metastasis. *Dev. Cell* **40**, 278–288.e5 (2017).
14. M. Biancospino et al., Clathrin light chain A drives selective myosin VI recruitment to clathrin-coated pits under membrane tension. *Nat. Commun.* **10**, 4974 (2019).
15. H. Maib, F. Ferreira, S. Vassilopoulos, E. Smythe, Cargo regulates clathrin-coated pit invagination via clathrin light chain phosphorylation. *J. Cell Biol.* **217**, 4253–4266 (2018).
16. J. C. Stachowiak, F. M. Brodsky, E. A. Miller, A cost-benefit analysis of the physical mechanisms of membrane curvature. *Nat. Cell Biol.* **15**, 1019–1027 (2013).
17. J. A. Ybe et al., Light chain C-terminal region reinforces the stability of clathrin heavy chain trimers. *Traffic* **8**, 1101–1110 (2007).
18. D. S. Chu, B. Pishvaee, G. S. Payne, The light chain subunit is required for clathrin function in Saccharomyces cerevisiae. *J. Biol. Chem.* **271**, 33123–33130 (1996).
19. J. D. Wilbur et al., Conformation switching of clathrin light chain regulates clathrin lattice assembly. *Dev. Cell* **18**, 841–848 (2010).
20. D. H. Wong et al., Neuron-specific expression of high-molecular-weight clathrin light chain. *J. Neurosci.* **10**, 3025–3031 (1990).
21. P. N. Dannhauser et al., Effect of clathrin light chains on the stiffness of clathrin lattices and membrane budding. *Traffic* **16**, 519–533 (2015).
22. M. Lherbette, L. Redlingshöfer, F. M. Brodsky, I. A. T. Schaap, P. N. Dannhauser, The AP2 adaptor enhances clathrin coat stiffness. *FEBS J.* **286**, 4074–4085 (2019).
23. C. Y. Chen, F. M. Brodsky, Huntingtin-interacting protein 1 (Hip1) and Hip1-related protein (Hip1R) bind the conserved sequence of clathrin light chains and thereby influence clathrin assembly in vitro and actin distribution in vivo. *J. Biol. Chem.* **280**, 6109–6117 (2005).
24. J. D. Wilbur et al., Actin binding by Hip1 (huntingtin-interacting protein 1) and Hip1R (Hip1-related protein) is regulated by clathrin light chain. *J. Biol. Chem.* **283**, 32870–32879 (2008).
25. A. M. Schreij et al., LRRK2 localizes to endosomes and interacts with clathrin-light chains to limit Rac1 activation. *EMBO Rep.* **16**, 79–86 (2015).
26. J. E. Heuser, T. S. Reese, Evidence for recycling of synaptic vesicle membrane during transmitter release at the frog neuromuscular junction. *J. Cell Biol.* **57**, 315–344 (1973).
27. S. Watanabe et al., Clathrin regenerates synaptic vesicles from endosomes. *Nature* **515**, 228–233 (2014).
28. S. Watanabe, E. Boucrot, Fast and ultrafast endocytosis. *Curr. Opin. Cell Biol.* **47**, 64–71 (2017).
29. S. F. Soukup, R. Vanhauwaert, P. Verstreken, Parkinson's disease: Convergence on synaptic homeostasis. *EMBO J.* **37**, e98960 (2018).
30. S. J. Koo et al., Vesicular synaptobrevin/VAMP2 levels guarded by AP180 control efficient neurotransmission. *Neuron* **88**, 330–344 (2015).
31. M. Cao et al., Parkinson Sac domain mutation in synaptojanin 1 impairs clathrin uncoating at synapses and triggers dystrophic changes in dopaminergic axons. *Neuron* **93**, 882–896.e5 (2017).
32. I. Milosevic et al., Recruitment of endophilin to clathrin-coated pit necks is required for efficient vesicle uncoating after fission. *Neuron* **72**, 587–601 (2011).
33. N. L. Kononenko et al., Clathrin/AP-2 mediate synaptic vesicle reformation from endosome-like vacuoles but are not essential for membrane retrieval at central synapses. *Neuron* **82**, 981–988 (2014).
34. Y.-I. Yim et al., Endocytosis and clathrin-uncoating defects at synapses of auxilin knockout mice. *Proc. Natl. Acad. Sci. U.S.A.* **107**, 4412–4417 (2010).
35. T. Mitsunari et al., Clathrin adaptor AP-2 is essential for early embryonal development. *Mol. Cell. Biol.* **25**, 9318–9323 (2005).
36. A. Musacchio et al., Functional organization of clathrin in coats: Combining electron cryomicroscopy and X-ray crystallography. *Mol. Cell* **3**, 761–770 (1999).
37. K. L. Morris et al., Cryo-EM of multiple cage architectures reveals a universal mode of clathrin self-assembly. *Nat. Struct. Mol. Biol.* **26**, 890–898 (2019).
38. W. K. den Otter, M. R. Renes, W. J. Briels, Self-assembly of three-legged patchy particles into polyhedral cages. *J. Phys. Condens. Matter* **22**, 104103 (2010).
39. A. Fotin et al., Molecular model for a complete clathrin lattice from electron cryomicroscopy. *Nature* **432**, 573–579 (2004).
40. F. Baschieri et al., Frustrated endocytosis controls contractility-independent mechanotransduction at clathrin-coated structures. *Nat. Commun.* **9**, 3825 (2018).
41. S. Schein, Architecture of clathrin fullerene cages reflects a geometric constraint—the head-to-tail exclusion rule—and a preference for asymmetry. *J. Mol. Biol.* **387**, 363–375 (2009).
42. F. K. Winkler, K. K. Stanley, Clathrin heavy chain, light chain interactions. *EMBO J.* **2**, 1393–1400 (1983).
43. P. K. Nandi, H. T. Pretorius, R. E. Lippoldt, M. L. Johnson, H. Edelhoch, Molecular properties of the reassembled coat protein of coated vesicles. *Biochemistry* **19**, 5917–5921 (1980).
44. P. P. Van Jaarsveld, P. K. Nandi, R. E. Lippoldt, H. Saroff, H. Edelhoch, Polymerization of clathrin protomers into basket structures. *Biochemistry* **20**, 4129–4135 (1981).
45. J. Heuser, T. Kirchhausen, Deep-etch views of clathrin assemblies. *J. Ultrastruct. Res.* **92**, 1–27 (1985).
46. E. Ungewickell, H. Ungewickell, Bovine brain clathrin light chains impede heavy chain assembly in vitro. *J. Biol. Chem.* **266**, 12710–12714 (1991).
47. B. Greene, S. H. Liu, A. Wilde, F. M. Brodsky, Complete reconstitution of clathrin basket formation with recombinant protein fragments: Adaptor control of clathrin self-assembly. *Traffic* **1**, 69–75 (2000).
48. S.-H. Liu, M. L. Wong, C. S. Craik, F. M. Brodsky, Regulation of clathrin assembly and trimerization defined using recombinant triskelion hubs. *Cell* **83**, 257–267 (1995).
49. P. N. Dannhauser, E. J. Ungewickell, Reconstitution of clathrin-coated bud and vesicle formation with minimal components. *Nat. Cell Biol.* **14**, 634–639 (2012).
50. O. Avinoam, M. Schorb, C. J. Beese, J. A. G. Briggs, M. Kaksonen, Endocytic sites mature by continuous bending and remodeling of the clathrin coat. *Science* **348**, 1369–1372 (2015).
51. B. L. Scott et al., Membrane bending occurs at all stages of clathrin-coat assembly and defines endocytic dynamics. *Nat. Commun.* **9**, 419 (2018).
52. S. Watanabe et al., Ultrafast endocytosis at mouse hippocampal synapses. *Nature* **504**, 242–247 (2013).
53. L. E. Dobrunz, Release probability is regulated by the size of the readily releasable vesicle pool at excitatory synapses in hippocampus. *Int. J. Dev. Neurosci.* **20**, 225–236 (2002).
54. J. F. Wesseling, D. C. Lo, Limit on the role of activity in controlling the release-ready supply of synaptic vesicles. *J. Neurosci.* **22**, 9708–9720 (2002).
55. C. F. Stevens, J. H. Williams, Discharge of the readily releasable pool with action potentials at hippocampal synapses. *J. Neurophysiol.* **98**, 3221–3229 (2007).
56. L. E. Dobrunz, C. F. Stevens, Heterogeneity of release probability, facilitation, and depletion at central synapses. *Neuron* **18**, 995–1008 (1997).
57. R. S. Zucker, W. G. Regehr, Short-term synaptic plasticity. *Annu. Rev. Physiol.* **64**, 355–405 (2002).

BIOCHEMISTRY

58. H. Shiotsuki et al., A rotarod test for evaluation of motor skill learning. J. Neurosci. Methods **189**, 180–185 (2010).

59. S. Stamm et al., Clathrin light chain B: Gene structure and neuron-specific splicing. Nucleic Acids Res. **20**, 5097–5103 (1992).

60. T. Kirchhausen, S. C. Harrison, P. Parham, F. M. Brodsky, Location and distribution of the light chains in clathrin trimers. Proc. Natl. Acad. Sci. U.S.A. **80**, 2481–2485 (1983).

61. S. R. Majeed et al., Clathrin light chains are required for the gyrating-clathrin recycling pathway and thereby promote cell migration. Nat. Commun. **5**, 3891 (2014).

62. S. L. Acton, F. M. Brodsky, Predominance of clathrin light chain LCb correlates with the presence of a regulated secretory pathway. J. Cell Biol. **111**, 1419–1426 (1990).

63. H. Heerssen, R. D. Fetter, G. W. Davis, Clathrin dependence of synaptic-vesicle formation at the Drosophila neuromuscular junction. Curr. Biol. **18**, 401–409 (2008).

64. K. Sato et al., Differential requirements for clathrin in receptor-mediated endocytosis and maintenance of synaptic vesicle pools. Proc. Natl. Acad. Sci. U.S.A. **106**, 1139–1144 (2009).

65. V. Poupon et al., Clathrin light chains function in mannose phosphate receptor trafficking via regulation of actin assembly. Proc. Natl. Acad. Sci. U.S.A. **105**, 168–173 (2008).

66. D. M. Valenzuela et al., High-throughput engineering of the mouse genome coupled with high-resolution expression analysis. Nat. Biotechnol. **21**, 652–659 (2003).

67. I. S. Näthke et al., Folding and trimerization of clathrin subunits at the triskelion hub. Cell **68**, 899–910 (1992).

68. F. M. Brodsky, Clathrin structure characterized with monoclonal antibodies. I. Analysis of multiple antigenic sites. J. Cell Biol. **101**, 2047–2054 (1985).

69. L. Ciani et al., Wnt signalling tunes neurotransmitter release by directly targeting Synaptotagmin-1. Nat. Commun. **6**, 8302 (2015).